Impact of water quality on Single Photon Avalanche Diode direct time-of-flight imaging

Joyce Mau
Defence Science Technology Group
Edinburgh, Australia
ManChing.Mau@dst.defence.gov.au

Vladimyros Devrelis
Ballistic Systems Pty Ltd
Edinburgh, Australia
vladimyros.devrelis@dst.defence.gov.au

Geoffrey Day
Defence Science Technology Group
Edinburgh, Australia
Geoff.Day@dst.defence.gov.au

Jochen Trumpf
Software Innovation Institute
Australian National University
Canberra, Australia
jochen.trumpf@anu.edu.au

Dennis Delic
Defence Science Technology Group
Edinburgh, Australia
Dennis.Delic@dst.defence.gov.au

***Abstract*—A detailed study on the effect of chlorophyll and sediment, two of the main constituents of ocean water on the image quality of a Single Photon Avalanche Diode (SPAD) direct time-of-flight (dToF) imaging system is conducted. This system consists of a 532nm laser and a 32x32 SPAD time-of-flight sensor. The degradation of laser power and the volume scattering function (VSF) are measured and the image quality of underwater objects imaged by the SPAD 32x32 time-of-flight sensor is examined. Classification accuracy of simple geometric shapes is used as an indicator of the quality of the SPAD images. Under lab conditions, controlled amounts of sediment and chlorophyll are added into a water tank for these experiments. The laser's output to input power ratio is found to be exponentially decreasing with increasing path length travelled by the beam. The laser's beam attenuation coefficient is calculated and found to increase linearly with increasing concentration of these constituents. Likewise, the volume scattering function of the beam is found to be larger when these two constituents are present in the water. All of these experimental results are in accordance with the predictions of the Beer-Lambert Law. Furthermore, the shape classification accuracy is shown to decrease with increasing concentrations of sediment. Overall, these results confirm that the quality of underwater images taken by the SPAD flash imaging system will rapidly degrade with increasing chlorophyll and sediment concentration.**

***Index Terms*—attenuation coefficient, detection, classification, volume scattering function, SPAD**

I. Introduction

3D imaging has applications for remote surveillance in the ocean, such as for use on autonomous underwater vehicles (AUVs). Currently, direct time-of-flight (dToF) imaging is a popular method. It consists of a photosensitive sensor that measures the time for light emitted from a source takes to travel to a target. Wavelengths from the visible light range are commonly used because they have the lowest attenuation in water. However, the various constituents in the ocean degrade the quality of these images. Suspended particles cause scattering, while organic matter reduces optical power.

At the moment, literature studies are focussed on ocean water effects on laser power, volume scattering function or image quality for dToF imaging. The ocean consists of mainly salt water with sediments and chlorophyll being the two major constituents. Various studies exist on the power attenuation of laser beams in clear salt water [1], [2]. As dToF imaging systems use a single wavelength, many studies choose a particular wavelength and investigate its power attenuation. These studies employ theoretical models [3] or physical experiments [4]. The attenuation effects of chlorophyll have been experimentally investigated for a 532nm laser using a tank of clear salt water with a predefined amount of chlorophyll [4]. Another study examined the attenuation of a 660nm laser beam in different chlorophyll concentrations to determine phytoplankton biomass in ocean water [5]. For sediments, studies use materials such as clay [6], Maalox [2] or a range of real sediments [7]. Additionally, the volume scattering function is important for understanding the laser's scattering profile which contributes to the noise levels images. A study [8] for a 514nm laser beam in three different turbidity levels of real ocean water has been reported. As for understanding the effect on images, studies have used targets such as corals [9], a mechanical fish [1], 3D shape objects that resemble underwater targets of interest [9], or a rectangular object with black, white and grey colours [6]. The sporadic nature of these studies makes it difficult to understand the real impact of the ocean on dToF imaging.

In this study, we perform a number of experiments in a lab-controlled environment to investigate the effects of different water conditions on a 532nm laser's power and the quality of a 32x32 Single Photon Avalanche Diode (SPAD) array dToF images. In particular, we measure the beam attenuation coefficient to understand the effect on the laser's power. The beam attenuation coefficient is defined as the limit of the spectral attenuation to the distance of photon travel as that distance becomes vanishingly small [10]. The literature often uses the terms beam attenuation coefficient and attenuation coefficient interchangeably. This coefficient is used in the Beer-Lambert Law to understand the amount of laser power at different transmitted distances [11]. Note that there are currently different versions of the Beer-Lambert Law used in the literature. The version referenced here is used in electro-optics, and a different version that is not formulated in terms of the beam attenuation coefficient is used in spectroscopy [12], [13]. From these two versions, we are able to deduce a linear relationship between the beam attenuation coefficient and increasing concentrations of chlorophyll and sediments, and provide experimental results to support the claim. This paper will also investigate the relative scattering shape of the laser travelling in different water conditions and present the result in the form of volume scattering functions. Furthermore, the quality of the dToF SPAD images will be examined by determining the performance of classifying geometric objects imaged by the SPAD system.

II. Contributions

In this paper, we examine the degradation of a continuous 532nm laser's power as well as a 32x32 SPAD array dToF sensor's image quality under lab-controlled water conditions. Fresh and salt water are tested with controlled amounts of chlorophyll and sediments. While studying the degradation in the laser's power, we determine the beam attenuation coefficient with increasing chlorophyll and sediment concentrations and find that it increases linearly. Secondly, we evaluate the ratio of output to input power for different path lengths and find that it decreases exponentially over distance. Finally, we measure the volume scattering function for the laser beam in different chlorophyll and sediment concentration conditions. Both of these results are in accordance with the predictions of the Beer-Lambert Law. In addition, we present the detection and classification results for SPAD images of targets with different shapes and colours. Viewed together, these results provide a good picture of the real impact of the ocean on SPAD dToF imaging.

III. Background

In this paper, we assume that the attenuation of light in all water conditions is uniform. Therefore, we can use the Beer-Lambert Law to calculate the beam attenuation coefficient.

The Beer-Lambert Law used in the electro-optics field is given in [11], and it is represented in this paper as follows:

$$\mu = -\frac{1}{x}log(\frac{I}{I_0}) \tag{1}$$

where μ (given in m^{-1}) is the beam attenuation coefficient, x is the path length (in m), I is the power intensity of the transmitted laser beam (in W) and I_0 is the power intensity of the incident laser beam (in W) [14]–[16].

In the field of spectroscopy, the Beer-Lambert Law is usually presented in the form given in [13] and is presented in this paper as follows:

$$A = -log\frac{I}{I_0} = \sigma x C \tag{2}$$

where A is absorbance, σ is the extinction coefficient, C is the substance's concentration in the sample and the remaining variables have the same meaning in (1). Equation (1) will be the version that is used in this paper.

From (1) and (2), we deduct that there is a linear relationship between the beam attenuation coefficient and the concentration of a substance:

$$\mu = \sigma C \tag{3}$$

IV. Methodology

The experiments reported in this paper are conducted in controlled water conditions in a water tank at the Australian Institute of Marine Science's (AIMS) SeaSim facility. All of these experiments are conducted in the dark to reduce the amount of noise and interference with measurements done in the water tank. The water tank is 4 meters by 1 meter by 0.75 meter in size. The tank has two acrylic portholes on one side (as shown in Fig. 1a) and they are 0.5m apart and are 0.12m in diameter each. The tank also has two large acrylic windows on one side as shown by Fig. 1b and Fig. 1c. Filtered sea water is used such that the residual particles are 1 μm in diameter or less. Sediments with diameters of 38 μm or less are used to increase the sediment concentration of the water in a controlled manner. Examples of the bottles of pre-mixed sediment solution are shown in Fig. 1d. For chlorophyll, a mixture of equal parts of six different microalgae are used to increase the chlorophyll concentrations of the tank water. Microalgae are used since they contain chlorophyll [18]. The microalgae used are Chaetoceros sp. (CS-256), Nanochloropsis oceania (CS-702), Isochrysis sp. (CS-177), Chaetoceros muelleri (CS-176), Dunaliella sp. (CS-353) and Rhodomonas salina (CS-24/01). These microalgae are between 3-10 μm in diameter.

A. Measuring the degradation of the power of a laser in 532nm wavelength

The power of a continuous 532nm laser beam before it enters the tank and after it exits the tank is measured for different path lengths in the water tank and for different water conditions. The input power of the laser beam equals the available power from the source. Therefore, a small proportion of the input laser beam is measured during the experiment to monitor the power fluctuations of the beam. A lens is used to focus the output beam onto a separate power sensor. Fig. 2a shows this setup. The two power sensors are connected to separate channels of the same power meter, a Newport Power Meter Model 2936-R. 10,000 measurements are taken for each power value and their average is used for the analysis. Fig. 2b shows an example of the laser beam transmitting through clear ocean water, where a mirror is used to reflect the laser beam to exit through the other porthole. Up to 5 mirrors are used in this experiment to vary the path lengths. Fig. 2c shows the aluminium mirrors used. In this paper, we assume there is negligible loss in laser power from mirror reflection. Since we are interested in the transmission of light in water, corrections

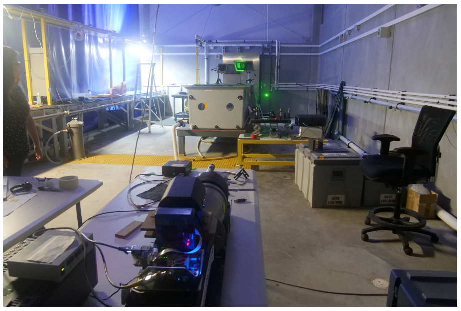

(a)

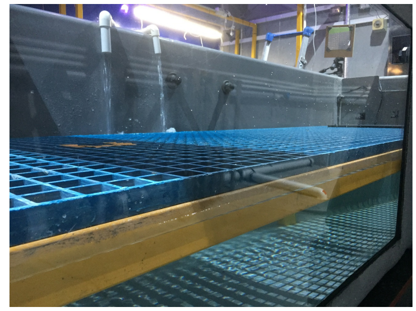

(b)

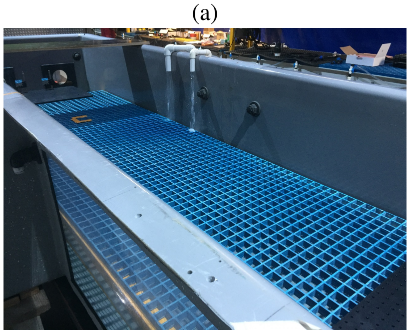

(c)

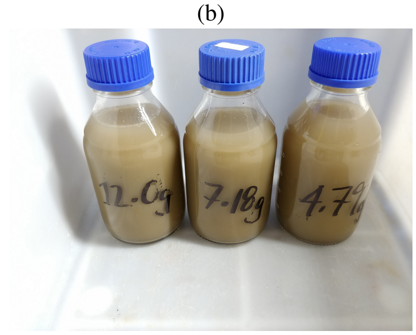

(d)

Fig. 1: (a) Tank setup in the lab room. [17] (b) View of the side window closer to the portholes. There are two large side windows on the right side of the tank. The tank is also being filled with clear fresh water here. (c) View of the side window further from the portholes. There are two large side windows on the right side of the tank. The tank is also being filled with clear fresh water here. (d) Sediment solutions used to increase sediment concentrations.

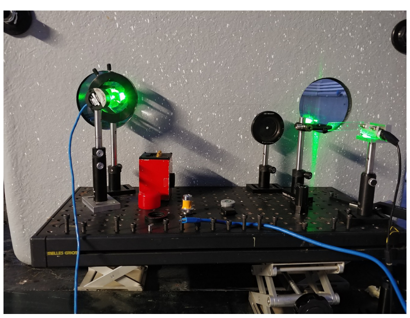

(a)

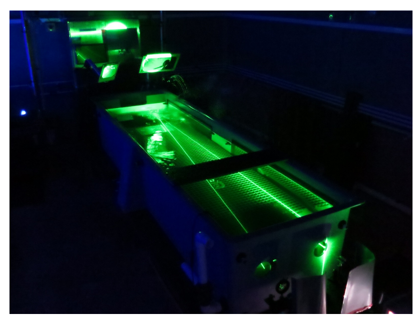

(b)

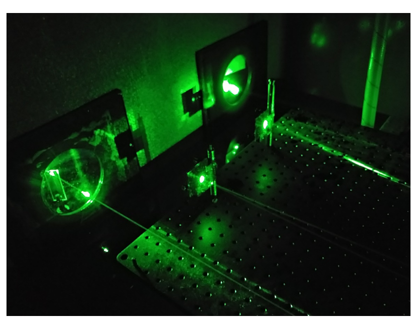

(c)

Fig. 2: (a) Setup outside the portholes to measure the input and output power of the laser beam. A small proportion of the input laser beam is diverted to a power meter during the experiment to monitor the power fluctuations of the beam. The output power is focussed by a lens onto a separate power sensor. (b) Laser beam transmitting through clear ocean water. (c) Mirrors used to reflect the laser beam to increase the transmitted length.

(a) (b)

Fig. 3: (a) Setup for measuring forward scattering. (b) Setup to measure backscatter, the beam is coming from the right and then reflected by the mirror to create a perpendicular beam pointing away from the side window for backscatter measurements.

are made in the transmitted intensities for the reflection losses through the acrylic portholes.

The recorded values are analysed in different ways to determine the different relationships shown in Section V. For the beam attenuation coefficient, the electro-optics version of the Beer-Lambert Law (see (1) in Section III) is used to calculate the experimental power and path length data. The conditions are clear fresh water, clear salt water, different amounts of additional sediments and different amounts of additional microalgae (which acts as chlorophyll). Using the same water tank as well as the same water, chlorophyll and sediment sources allow comparisons to be made with a high level of confidence.

B. Measuring the volume scattering function

For the volume scattering function (VSF), the backward and forward scattered powers are measured by the 32x32 SPAD array direct time-of-flight camera from Polimi in photon counting mode. The lens used is a Computar 50mm 1.3. Both the laser and SPAD camera are positioned outside the tank next to the side window closer to the porthole. The laser beam is transmitted into the water tank and then it is directed around the tank using mirrors. The beam is pointed perpendicular towards the SPAD camera's plane of view when measuring forward scattering. A small circular piece of black masking tape is cut out to just cover the incident beam so only the scattered power is imaged by the camera. This setup is shown in Fig. 3a. For backward scattering, the beam is pointed perpendicularly away from the SPAD camera's plane of view as shown in 3b. The scattered power is determined by summing up the photon counts of all the 32x32 pixels. The camera is moved at incremental angles of 5 degrees between 0 to 85 degrees left of the laser beam. The scattering power of only one side is measured because we assume that the scattering is symmetric along the laser beam. Also, the scattering powers at 85 to 90 degrees are not measured due to the physical limitations of the water tank. Over a thousand images are taken for each scattering power measurement so averaging can be applied to reduce error. As images at certain angles appear brighter due to more scattering, the F-number of the lens is adjusted to prevent saturation in photon counts by the SPAD camera. The F-number is defined as the ratio of the effective focal length to the aperture diameter [19]. As the same lens is used for all photon counting measurements, the F-number only affects the size of the aperture diameter which directly relates to the amount of photons received by the sensor. In this experiment, we are only interested in the shape of the scattering hence we are determining the relative scattered power between different angles. This can be achieved by correcting all the photon counting measurements to one standard F-number by using (4) below:

$$P_n = \frac{F_i}{F_n} P_i \tag{4}$$

where P is the total number of photons, F is the F-number, the subscript n stands for the normalised version, and the subscript i stands for the version used for the measurement. Results in Section V-A will list which value is used for each volume scattering function plot.

C. Classification of underwater objects imaged by the SPAD system

To understand whether detection and classification is possible for SPAD images of underwater targets, simple geometric shapes are selected as the baseline performance indicator. Specifically, three thin plastic shapes spray painted in matte grey (shown in Fig. 4a) are used. All three shapes fit within a square with a side length of 400mm. These shapes are attached to the top of an optical mount that is 1220mm in height and is placed at 2.91m away from the portholes. Fig. 4b shows the laser illuminating a triangle in the water that is placed higher in the water by the optical mount on the left. To obtain images of each shape, the SPAD flash system images through the portholes. The camera used is a DST-developed 32x32 SPAD array and the laser used is a pulsing 532nm laser. The camera and laser are placed 150mm apart with the camera pointing at the left porthole from a distance of 5.11m and the laser pointing through the right porthole from a distance of 5.03m. Fig. 4d shows the processed frames, where a circle is imaged instead of a triangle in this image and the optical mount is seen on the left.

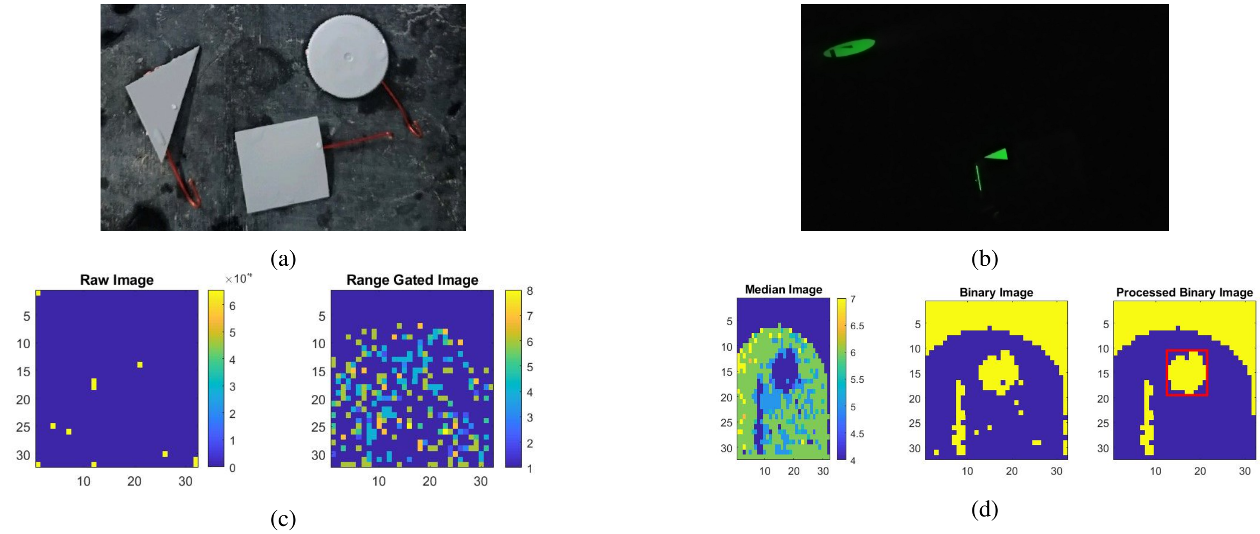

Fig. 4: (a) The thin plastic shapes spray painted in matte grey used for imaging in this paper. Note they have a wire hook attached so they can be attached to the optical mount. (b) The grey right angle triangle in the water being illuminated by the laser beam during calibration. (c) Comparison of one frame of raw image (left) to one frame of range-gated image (right) (sediment concentration: 1.2 mg/L). Range gating restricted the displayed clock cycles to 1 to 8 as seen on the colour bar. The pixels with values outside this range is shown as the dark blue. This enables more pixels to be seen because the smaller range highlights the smaller differences between values in this range. The large dark blue area on the top of the image is due to the acrylic porthole blocking the laser illumination, hence the clock cycle will be outside the range. (d) Processing a median image to a binary image for detection (sediment concentration: 1.2 mg/L). There are no returns at the top of these images for the same reason as Fig. 4c.

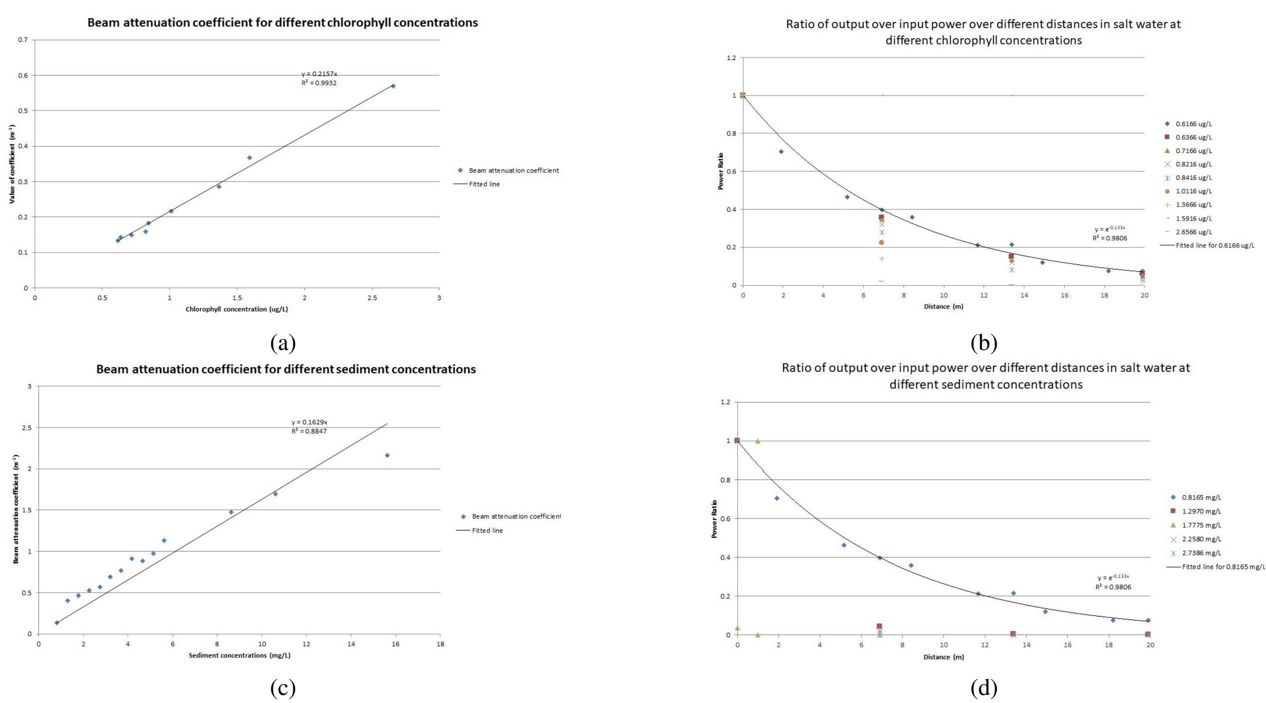

Fig. 5: (a) The attenuation coefficient's relationship with different concentrations of chlorophyll. (b) The fitted plot corresponds to the power ratios for clear sea water. An estimate of 0.6166 $\mu g/L$ is made to account for the residual chlorophyll in clear sea water. The other data points correspond to different chlorophyll concentrations. (c) The attenuation coefficient's relationship with different concentrations of sediment. (d) The fitted plot corresponds to the power ratios for clear sea water. An estimate of 0.8165 mg/L is made to account for the residual sediment in clear sea water. The other data points correspond to different sediment concentrations.

In this paper, a binary image is used for detection and classification. Fig. 4c and Fig. 4d show images at each of the processing stages from raw to binary image. Range gating is used as shown in Fig. 4c to enable better analysis of the variation of distance values within the known distance range of the shape, which is 1 to 8 clock cycles in this figure. Afterwards, a median image is computed for a running 200 frames and then the 5th percentile of the median image is used as the threshold value for converting the image to a binary image. The 5th percentile is chosen because the shape's distance was in this percentile. Finally, scattered pixels are removed and holes are filled to produce an image suitable for detection as shown in the leftmost image in Fig. 4d. Detection is performed using Matlab's `regionprops` function which draws a bounding box around any detected objects. As this is a common detection algorithm, the results presented in this paper will focus on the classification performance only. Many objects are detected by this function hence a series of rules on the bounding box's area, aspect ratio and position is used to remove all objects that are not the target shape. For classification, a set of rules on the shape's area and the ratio of the shape's area to the bounding box's area is used for differentiating the shapes. These rules are developed by [20] but the threshold values to classify shapes are different in this paper as the images of shapes have less sharp edges as the images in [20]. The classifier also has a prediction class called unknown for the cases where the shape can not be uniquely determined.

V. Results

Two different types of relationships are plotted using the power measurements made for increasing concentrations of chlorophyll and sediments (see Fig 5). During the data analysis, an estimate is made to account for the residual chlorophyll and sediments in the clear ocean water. The estimate is obtained through an iterative adjustment between beam attenuation coefficient and concentration to ensure a linear relationship and on the assumption that the coefficient value is zero for zero concentration. Firstly, the values of the beam attenuation coefficient for different concentrations of chlorophyll (see Fig. 5a) and sediments (see Fig. 5c) are plotted. The coefficient value plotted on the graph is an average of coefficient values calculated from the output and input powers measured at different distances. The trend lines in both figures are linear, which is in accordance with the predictions of (3) in Section III. Secondly, the relationship between the ratio of output to input power with increasing distance is plotted for chlorophyll (see Fig. 5b) and sediments (see Fig. 5d). The different sets of coloured data points represent the measurements made at different concentrations. We assume that there is no power loss when the light has travelled zero distance so an extra data point is added at zero distance with a power ratio of 1. The trend line for clear ocean water confirms (1) in Section III and the shift for different concentrations agrees with the predictions of both versions of the Beer-Lambert Law (see (1) and (2) from Section III).

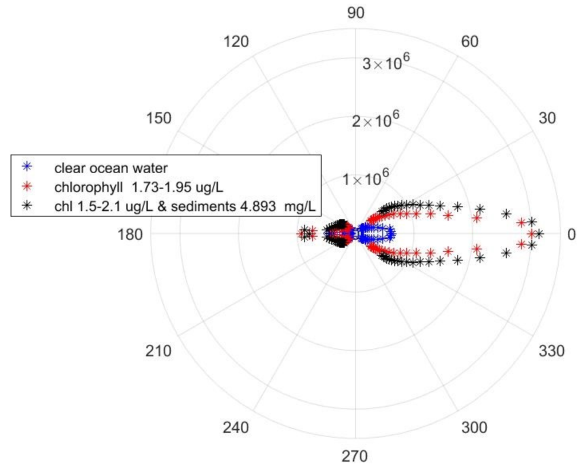

Fig. 6: Comparison of volume scattering functions in different water conditions.

A. Volume Scattering Function

Fig. 6 shows the volume scattering functions at different angles in different water conditions. The values are the summed photon counts of the average frame over all the frames recorded for each angle. The shape shows that Mie scattering is present for all conditions, where the scattering is much smaller for clear ocean water since the residual particles are below $1\mu m$, while the other two conditions causes a larger scattering shape as the sediments and micro-algae are much larger. This all fits with the theory of Mie scattering [21], [22]. Also, as the scattering coefficient is part of the sum for beam attenuation coefficient [23], the larger scattering power also agrees with the predictions of (3). Furthermore, the scattering powers are lower around 50-85 and 275-310 degrees because much of the scattered light is refracted by the acrylic window at these angles. There are no data points for the angles 85-95 and 265-275 degrees for the reasons stated in Section IV-B,. The standardised F-number (as mentioned in Section IV-B) used is 1.8, since the backscatter is measured with a F-number of 1.8 and the forward scatter is measured with a F-number of 5.6. Reducing the amount of light reduces measurement errors. Since the backscatter light is partially blocked by the mirror as described in the setup in Section IV-B and shown in Fig. 3b, the values between 175 to 185 are manually increased to compensate for the blocked light. The values are doubled for all angles in this range except for 180, where it is tripled. The increase is determined manually to fit in with the rest of the backscatter shape.

B. Effects of varying sediment concentration on classifying shapes

Our analysis is focussed on classification since the methods used for detection are common, as discussed in Section IV-C. Images of a circle, a triangle or a square in varying amounts of sediment concentrations are tested for classification using the algorithm as described in Section IV-C. The overall accuracies

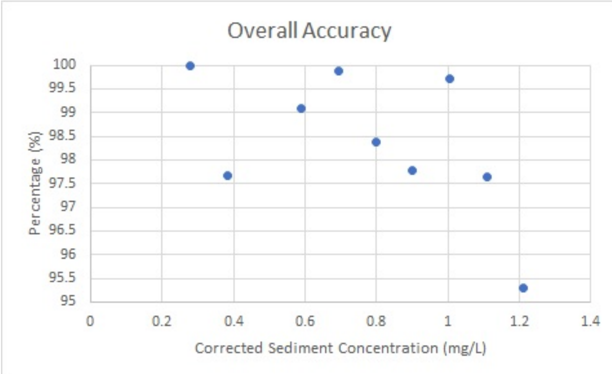

Fig. 7: Overall accuracy in classifying SPAD images of a circle, a square or a triangle in varying sediment concentrations.

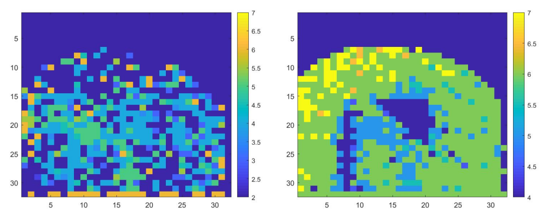

(a) (b)

Fig. 8: (a) A SPAD image of a triangle in 1.9 mg/L of sediments in ocean water. (b) A SPAD image of a triangle in 1.2 mg/L of sediments in ocean water.

in classifying for different concentrations are presented in Fig. 7. For each sediment concentration, the classification algorithm is tested on 900 binary images of each shape.

Classification works well up to a sediment concentration of 1.2 mg/L. For a higher concentration, different types of classifiers may need to be used. The F1-measure of the classification algorithm is above 97.5% for concentrations up to 1.3 mg/L and shows that the algorithm is quite balanced. Its macro precision and macro recall percentages are above 96% for this range of sediment concentrations. For concentrations greater than 1.8 mg/L, there is a high level of noise in the image such that the shape cannot be detected using the applied algorithm hence classification cannot be done. Other approaches will need to be considered. An example of a processed SPAD image of a triangle in 1.9 mg/L sediment concentrated ocean water is shown in Fig. 8a and it can be seen that the triangle is not clear in comparison to Fig. 8b which is a processed SPAD image of the same triangle in 1.2 mg/L sediment concentrated ocean water.

VI. Conclusion

In this paper, we experimentally measured the laser's output to input power ratio and found it exponentially decreases with increasing path lengths, and the ratios are lower for high concentrations of sediments or chlorophyll. These findings are in accordance with the predictions of the Beer-Lambert Law. We also confirmed the predictions of the same law by finding that the beam attenuation coefficient is linearly dependent on the different concentrations of chlorophyll and sediment. In addition, we examined the variation in the volume scattering function under different water conditions and the results agree with the Beer-Lambert Law as well. Lastly, we investigated the performance of detection and classification algorithms in analysing SPAD array images of different geometric shapes in different water conditions. Overall, these results confirm that there is a rapid degradation in laser power and shape as well as SPAD image quality with increasing concentration of sediment.

VII. Acknowledgements

The authors would like to thank Craig Humphrey and Tom Barker from the SeaSim facility and David Crossman and Melanie Olsen from the Australian Institute of Marine Science for assisting us with the experimental setup and allowing us to use their facilities. We would also like to acknowledge Dr Graeme Nash for assisting in the experimental design at the initial stage of the work.

References

[1] H. Merbold, G.-P. Catregn, and T. Leutenegger, "Time-of-flight range imaging for underwater applications," in *Proc. SPIE 10539, Photon. Instrum. Eng. V*, San Francisco, United States, Feb. 2018, p. 2. [Online]. Available: https://www.spiedigitallibrary.org/conference-proceedings-of-spie/10539/2283476/Time-of-flight-range-imaging-for-underwater-applications/10.1117/12.2283476.full

[2] A. Maccarone, A. McCarthy, X. Ren, R. E. Warburton, A. M. Wallace, J. Moffat, Y. Petillot, and G. S. Buller, "Underwater depth imaging using time-correlated single-photon counting," *Opt. Express 33911*, vol. 23, no. 26, p. 16, Dec. 2015.

[3] A. Kumar, S. Prince, N. Vedachalam, and V. D. Prakash, "Ocean water channel modeling and estimation of power link budget for underwater wireless link," in *2017 Int. Conf. Wireless Communications, Signal Processing and Networking (WiSPNET)*, Chennai, Mar. 2017, pp. 1369–1372.

[4] Y. J. Gawdi, "Underwater free space optics," North Carolina State University, Raleigh, North Carolina, Tech. Rep., 2006.

[5] M. J. Behrenfeld and E. Boss, "Beam attenuation and chlorophyll concentration as alternative optical indices of phytoplankton biomass," *J. Mar. Res.*, vol. 64, no. 3, pp. 431–451, May 2006. [Online]. Available: http://openurl.ingenta.com/content/xref?genre=article&issn=0022-2402&volume=64&issue=3&spage=431

[6] M. Benger *et al.*, "UTOFIA: an underwater time-of-flight image acquisition system," in *Proc. SPIE 10434, Electro-Opt. Remote Sens. XI*, Warsaw, Poland, Oct. 2017, p. 3. [Online]. Available: https://www.spiedigitallibrary.org/conference-proceedings-of-spie/10434/2277944/UTOFIA-an-underwater-time-of-flight-image-acquisition-system/10.1117/12.2277944.full

[7] E. T. Baker and J. W. Lavelle, "The effect of particle size on the light attenuation coefficient of natural suspensions," *J. Geophysical Research*, vol. 89, no. C5, p. 8197, 1984. [Online]. Available: http://doi.wiley.com/10.1029/JC089iC05p08197

[8] T. J. Petzold, "Volume scattering functions for selected ocean waters," Scripps Institution of Oceanography La Jolla Ca Visibility Lab, Fort Belvoir, VA, USA, Tech. Rep., Oct. 1972. [Online]. Available: http://www.dtic.mil/docs/citations/AD0753474

[9] S. T. Digumarti, G. Chaurasia, A. Taneja, R. Siegwart, A. Thomas, and P. Beardsley, "Underwater 3D capture using a low-cost commercial depth camera," in *2016 IEEE Winter Conf. Applications of Computer Vision (WACV)*, Lake Placid, NY, USA, Mar. 2016, pp. 1–9. [Online]. Available: http://ieeexplore.ieee.org/document/7477644/

[10] C. Mobley, "References-brief definitions," Aug. 2017. [Online]. Available: http://www.oceanopticsbook.info/view/references/brief_definitions

[11] F. G. Smith, *The infrared & electro-optical systems handbook - vol 2: atmospheric propagation of radiation*, J. S. Accetta and D. L. Shumaker, Eds. Michigan, United States and Bellingham, United States: Infrared Information Analysis Center, ERIM and SPIE Optical Engineering Press, 1993.

[12] J. Ingle Jr and S. R. Crouch, *Spectrochemical analysis*, 1st ed. New Jersey, United States: Prentice Hall, Mar. 1988.

[13] A. Tokmakoff, "Absorption cross-sections," Jun. 2019. [Online]. Available: https://chem.libretexts.org/Bookshelves/Physical_and_Theoretical_Chemistry_Textbook_Maps/Book%3A_Time_Dependent_Quantum_Mechanics_and_Spectroscopy_(Tokmakoff)/07%3A_Interaction_of_Light_and_Matter/7.05%3A_Absorption_Cross-Sections

[14] C. Roesler, "Absorption-measurement of absorption," Aug. 2017. [Online]. Available: http://www.oceanopticsbook.info/view/absorption/measurement_of_absorption

[15] F. D. Kashani, M. R. H. Rad, and E. Kazemian, "Analyzing the propagation behavior of a gaussian laser beam through seawater and comparing with atmosphere," *Iranian Journal of Elect. Electron. Eng.*, vol. 9, no. 4, p. 7, Dec. 2013.

[16] W. Gomaa, A. F. El-Sherif, and Y. H. El-Sharkawy, "Underwater laser detection system," in *Proc. SPIE 9342, Solid State Lasers XXIV*, San Francisco, California, United States, Mar. 2015, p. 934221. [Online]. Available: http://proceedings.spiedigitallibrary.org/proceeding.aspx?doi=10.1117/12.2080181

[17] AIMS SeaSim, "Lasers in SeaSim tanks," Sep. 2018. [Online]. Available: https://twitter.com/SeaSim_AIMS/status/1044060263656243201

[18] A. Hosikian, S. Lim, R. Halim, and M. K. Danquah, "Chlorophyll extraction from microalgae: a review on the process engineering aspects," *Int, J. Chemical Engineering*, vol. 2010, pp. 1–11, Mar. 2010. [Online]. Available: http://www.hindawi.com/journals/ijce/2010/391632/

[19] M. C. Dudzik, *The infrared & electro-optical systems handbook - vol. 4: electro-optical systems design, analysis, and testing*, J. S. Accetta and D. L. Shumaker, Eds. Michigan, United States and Bellingham, United States: Infrared Information Analysis Center, ERIM and SPIE Optical Engineering Press, 1993.

[20] S. V. Chhaya, S. Khera, and P. Kumar S, "Basic geometric shape and primary colour detection using image processing on matlab," *Int. J. Res. in Engin. and Technol.*, vol. 4, no. 5, pp. 505–509, May 2015. [Online]. Available: https://ijret.org/volumes/2015v04/i05/IJRET20150405094.pdf

[21] R. Nave, "Mie Scattering." [Online]. Available: http://hyperphysics.phy-astr.gsu.edu/hbase/atmos/blusky.html

[22] J. R. Meyer-Arendt, *Introduction to classical and modern optics*, 3rd ed. Englewood cliffs, United States: Prentice-Hall, 1989.

[23] C. Mobley, "Inherent Optical Properties," Feb. 2010. [Online]. Available: http://www.oceanopticsbook.info/view/overview_of_optical_oceanography/inherent_optical_properties